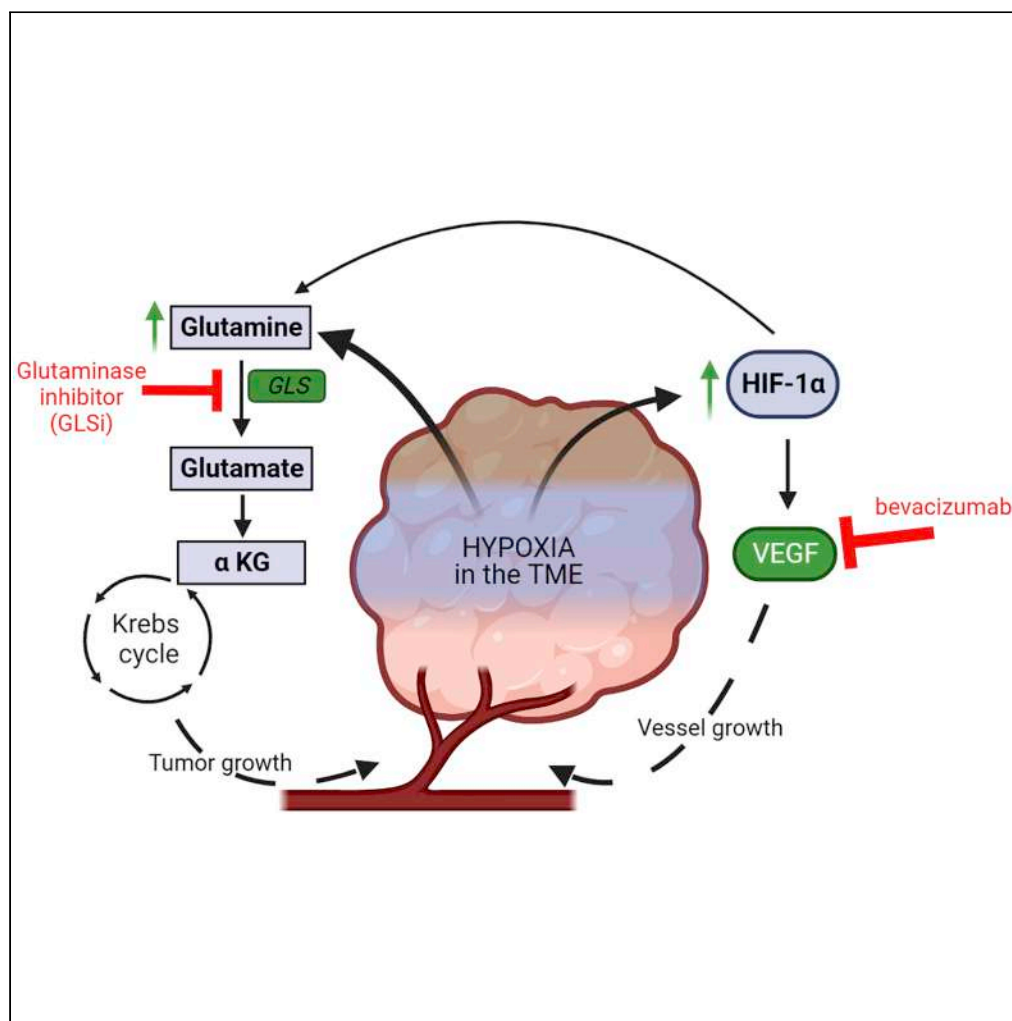


Article

Exploiting metabolic vulnerabilities after anti-VEGF antibody therapy in ovarian cancer



Deanna Glassman,
Mark S. Kim,
Meredith Spradlin,
..., Livia S. Eberlin,
Deepak Nagrath,
Anil K. Sood

asood@mdanderson.org

Highlights

Resistance to anti-vascular endothelial growth factor antibody (AVA) is common

We examine a small molecule inhibitor of glutaminase (GLSi) to combat resistance

GLSi enhanced the efficacy of AVA *in vitro* and *in vivo*, even in AVA-resistant tumors

This work supports further development of GLSi in AVA-resistant ovarian cancer

Glassman et al., iScience 26,
106020
February 17, 2023 © 2023 The
Authors.
[https://doi.org/10.1016/
j.isci.2023.106020](https://doi.org/10.1016/j.isci.2023.106020)

Article

Exploiting metabolic vulnerabilities after anti-VEGF antibody therapy in ovarian cancer

Deanna Glassman,¹ Mark S. Kim,¹ Meredith Spradlin,^{2,9} Sunil Badal,² Mana Taki,¹ Pratip Bhattacharya,³ Prasanta Dutta,³ Charles V. Kingsley,³ Katherine I. Foster,¹ Olamide Animasahun,^{4,5} Jin Heon Jeon,⁴ Abhinav Achreja,⁴ Anusha Jayaraman,⁴ Praveen Kumar,⁴ Minal Nenwani,⁴ Fulei Wuchu,⁴ Emine Bayraktar,¹ Yutuan Wu,¹ Elaine Stur,¹ Lingegowda Mangala,¹ Sanghoon Lee,^{1,6} Timothy A. Yap,^{7,8} Shannon N. Westin,¹ Livia S. Eberlin,^{2,9} Deepak Nagrath,⁴ and Anil K. Sood^{1,10,*}

SUMMARY

Despite modest clinical improvement with anti-vascular endothelial growth factor antibody (AVA) therapy in ovarian cancer, adaptive resistance is ubiquitous and additional options are limited. A dependence on glutamine metabolism, via the enzyme glutaminase (GLS), is a known mechanism of adaptive resistance and we aimed to investigate the utility of a GLS inhibitor (GLSi). Our *in vitro* findings demonstrated increased glutamine abundance and a significant cytotoxic effect in AVA-resistant tumors when GLSi was administered in combination with bevacizumab. *In vivo*, GLSi led to a reduction in tumor growth as monotherapy and when combined with AVA. Furthermore, GLSi initiated after the emergence of resistance to AVA therapy resulted in a decreased metabolic conversion of pyruvate to lactate as assessed by hyperpolarized magnetic resonance spectroscopy and demonstrated robust antitumor effects with a survival advantage. Given the increasing population of patients receiving AVA therapy, these findings justify further development of GLSi in AVA resistance.

INTRODUCTION

Ovarian cancer presents at late stages and is the most lethal gynecologic malignancy with more than 14,000 deaths per year.¹ The tumor microenvironment (TME) of ovarian cancer, like those of other solid tumors, is characterized by hypoxia and increased levels of vascular endothelial growth factor (VEGF) which promotes angiogenesis, tumor growth, and progression.^{2,3} While the mainstay of treatment of ovarian cancer consists of tumor-reductive surgery and chemotherapy,⁴ advances in therapy have been aimed at targeting angiogenesis.⁵ Treatment with bevacizumab, a humanized monoclonal antibody against VEGF, has resulted in modest improvements in progression-free survival^{6–8}; and it represents the first effective biologically targeted therapy for ovarian cancer. It is now approved by the U.S. Food and Drug Administration for use in both the up-front and recurrent settings.⁹ Practically speaking, this means that nearly all patients with ovarian cancer will be treated with anti-VEGF antibody (AVA) therapy at some point in their care. Unfortunately, the effects of this treatment are transient; virtually all tumors adapt a resistance to it and patients eventually succumb to their disease.¹⁰ Thus, alternative treatment strategies for AVA-resistant ovarian tumors represent a growing unmet clinical need.

Among the possible opportunities for overcoming adaptive resistance to AVA drugs, the dynamic changes in metabolism that are due, in part, to the hypoxic stress imposed by AVA therapy are considered here. In concert with elevated VEGF expression, tumor cells exhibit not only the Warburg effect with high rates of glucose consumption but also a dependence on glutamine metabolism, particularly with long-term exposure to bevacizumab.¹¹ Glutamine is an essential amino acid that plays a critical role in anaplerosis, cancer initiation, and progression. Metabolic utilization of glutamine requires conversion to glutamate via the enzyme glutaminase (GLS). Researchers have exploited glutamine dependence in clinical trials of the treatment of solid tumors with GLS inhibitors (GLSi) (clinicaltrials.gov).^{12–32} However, the role of GLSi in overcoming adaptive resistance to AVA therapy is not known. We therefore investigated the impact of

¹Department of Gynecologic Oncology and Reproductive Medicine, The University of Texas MD Anderson Cancer Center, Unit 1362, 1515 Holcombe Blvd, Houston, TX 77030, USA

²Department of Chemistry, The University of Texas at Austin, Austin, TX, USA

³Department of Cancer Systems Imaging, The University of Texas MD Anderson Cancer Center, Houston, TX, USA

⁴Department of Biomedical Engineering, University of Michigan, Ann Arbor, MI, USA

⁵Department of Chemical Engineering, University of Michigan, Ann Arbor, MI, USA

⁶Department of Systems Biology, The University of Texas MD Anderson Cancer Center, Houston, TX, USA

⁷Department of Investigational Cancer Therapeutics, The University of Texas MD Anderson Cancer Center, Houston, TX, USA

⁸The Institute for Applied Cancer Science, The University of Texas MD Anderson Cancer Center, Houston, TX, USA

⁹Department of Surgery, Baylor College of Medicine, Houston, TX, USA

¹⁰Lead contact

*Correspondence:

asood@mdanderson.org

<https://doi.org/10.1016/j.isci.2023.106020>



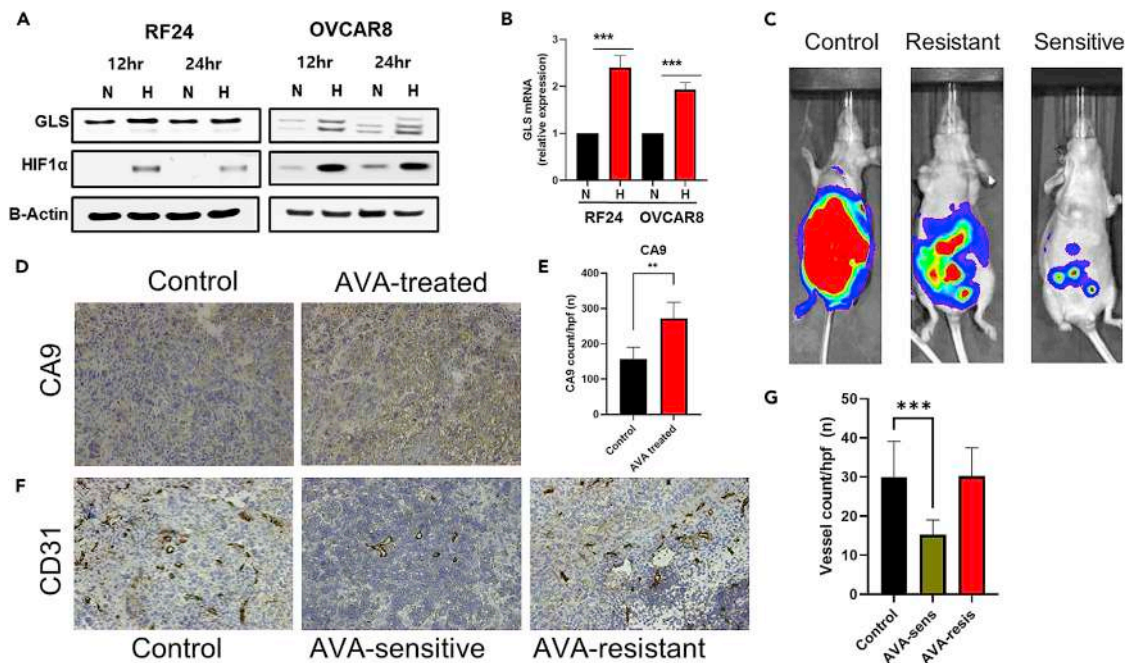


Figure 1. Metabolic alterations in hypoxia and resulting from AVA therapy

(A and B) RF24 and OVCAR8 cells were cultured in normoxia (N) or hypoxia (H) for 12 and 24 h. GLS and HIF-1 α protein (A) and GLS mRNA (B) expression levels in both cell lines were measured. Error bars indicate SD, *** $p < 0.001$.

(C) Images of nude mice inoculated with 1×10^6 SKOV3ip1 cells and given bevacizumab (6.25 mg/kg twice weekly) until resistance emerged.

(D) IHC staining of frozen mouse ovarian tumors for the hypoxia marker CA9 in control vs. bevacizumab-treated (AVA-treated) tumors.

(E) Quantification of CA9 staining in control vs. AVA-treated tumors per high power field, error bars indicate SD ** $p < 0.01$.

(F) IHC staining of frozen mouse ovarian tumors for endothelial cell marker CD31 in control vs. AVA-sensitive or AVA-resistant tumors.

(G) Quantification of vessel densities in control, AVA-sensitive, and AVA-resistant tumor samples. Error bars indicate SD. *** $p < 0.001$ compared with the control group (Student's t test). AVA, anti-VEGF antibody (bevacizumab); AVA-sens, AVA-sensitive; AVA-resis, AVA-resistant.

inhibiting GLS in the setting of glutamine dependence experienced by tumors under hypoxic stress imposed by AVA therapy. We hypothesize that hypoxia-mediated glutamine dependence in AVA-resistant ovarian cancer will make it susceptible to GLS inhibition.

RESULTS

Treatment with, and adaptive resistance to, AVA therapy induces alterations in glutamine metabolism

Due to the abnormal vasculature inherent in tumors during malignant growth, the physiologic oxygen tension of solid tumors is hypoxic (1%–2%) compared to the surrounding parenchyma.³³ Additional hypoxic stress to the tumor is imposed by treatment with AVA therapy (i.e. bevacizumab). After prolonged AVA exposure, tumor oxygen tension levels are estimated to be lower than 1%³³ and we therefore set out to understand the impact of hypoxia extremes on glutamine metabolism. To do so, we first evaluated *in vitro* GLS expression in the ovarian cancer cell line OVCAR8 and immortalized endothelial cell line RF24 at 1% oxygen (aka hypoxic) conditions. We did this in concert with measuring the hypoxia-inducible factor-1 alpha (HIF-1 α) expression level. We identified that GLS and HIF-1 α expression in both cell lines was higher under hypoxic rather than under normoxic conditions (Figures 1A and 1B).

To evaluate the downstream metabolic effects of altered GLS expression, we performed an *in vivo* investigation using an orthotopic SKOV3ip1 model of ovarian cancer with adaptive resistance to AVA therapy with bevacizumab. In this experiment, mice received either a vehicle control or AVA therapy and all AVA-treated mice underwent weekly bioluminescent imaging in order to stratify them based on sensitivity or resistance to AVA therapy as outlined in the Materials and Methods (Figure 1C). We harvested tumors after they became resistant to treatment and assessed markers of hypoxic stress using immunohistochemical (IHC) staining. Compared with control tumors, all AVA-treated tumors had higher levels of the hypoxia

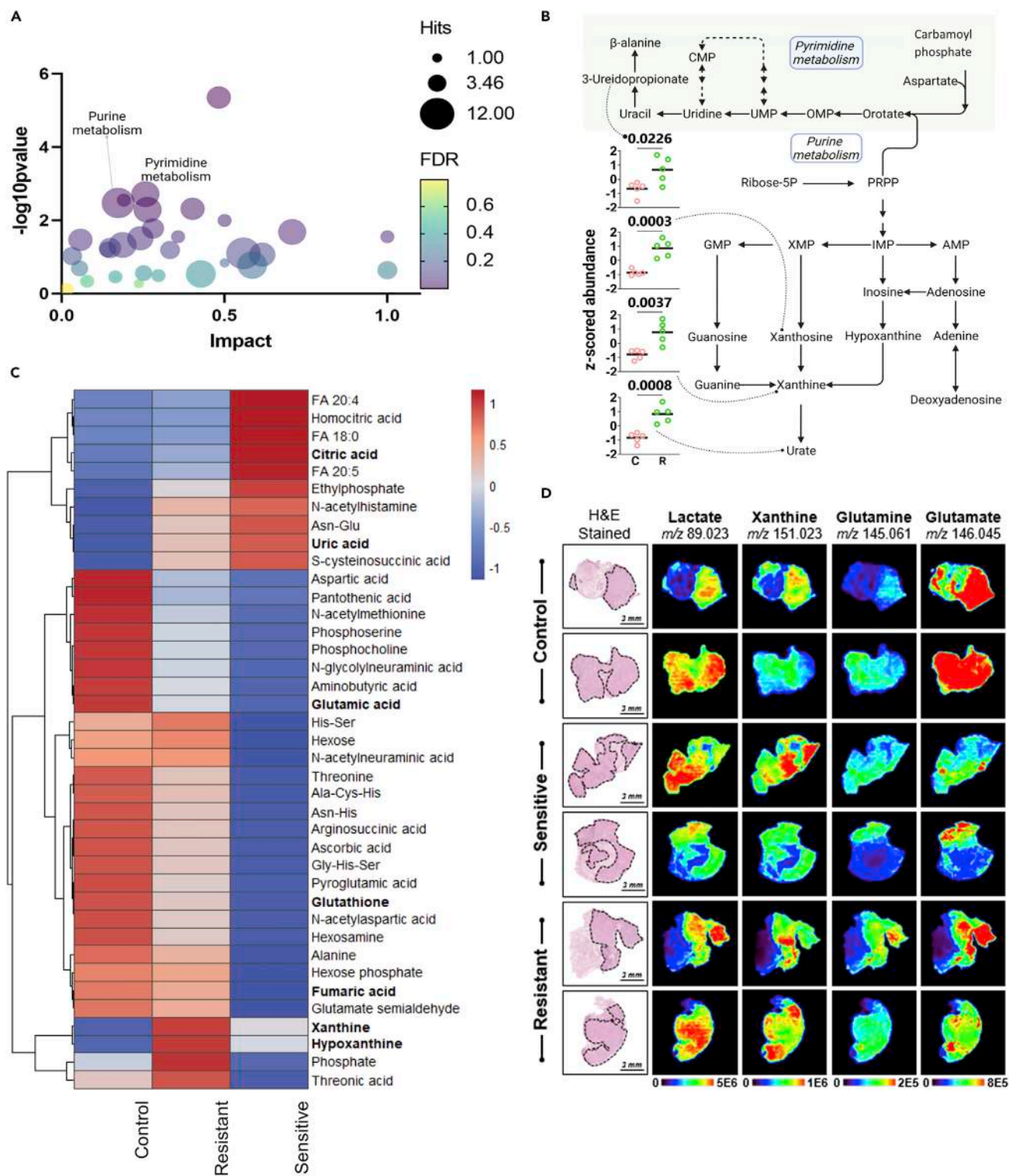


Figure 2. Adaptive resistance of ovarian cancer to AVA therapy induces alterations in glutamine metabolism

(A) Plot of metabolic pathway impact analysis results after quantitative metabolic analysis by LC-MS of ovarian tumor from an orthotopic mouse model with SKOV3ip1 cells comparing control vs. AVA-resistant groups showing that the purine and pyrimidine metabolism differed markedly (FDR < 0.05). Data were generated using a MetaboAnalyst plot made with Prism software.

Figure 2. Continued

(B) Simplified diagram of the purine and pyrimidine metabolic pathways showing the key metabolites involved in purine and pyrimidine nucleotide metabolism. The inserted scatterplots show significantly higher levels of downstream metabolites indicated in the dashed arrow lines (urate, xanthine, xanthosine, and 3-ureidopropionate) in the resistant group (R) than in the control group (C), $p < 0.05$. UMP, uridine monophosphate; OMP, orotidine 5'-monophosphate; CMP, cytidine monophosphate; PRPP, phosphoribosyl pyrophosphate; GMP, guanosine monophosphate; XMP, xanthosine monophosphate; IMP, inosine monophosphate; AMP, adenosine monophosphate. Key intermediates in amino acid metabolism, glycolysis, and purine synthesis are indicated in bold.

(C) Intensity heatmap for metabolites selected by SAM as significantly altered among control, AVA-resistant, and AVA-sensitive tissues (FDR <5%) identified by DESI-MS imaging. Features were clustered using a Euclidean-distance formula according to the average signal intensity of the corresponding m/z value measured from tumor-specific regions. The color scale reflects Z score standard deviations from the mean relative abundance measured for each ion. For fatty acid (FA) species, X:Y indicates the number of carbons and double bonds, respectively.

(D) DESI-MS images showing an increase in glutaminolysis in AVA-treated tumors compared to control tumors, with an increased relative abundances of glutamate relative to glutamine in AVA-resistant compared to AVA-sensitive tissues and a decreased abundance of glutamate and glutamine in all AVA-treated tumors.

marker CA9 ($p < 0.01$, Figures 1D and 1E) and the AVA-sensitive tumors demonstrated lower levels of the endothelial cell marker CD31 compared with those that were resistant to AVA treatment ($p < 0.001$, Figures 1F and 1G).

After confirming that AVA therapy results in hypoxic stress, we set out to define the specific alterations in tumor metabolism that occur in response to this stress. We first performed a quantitative metabolic analysis of the AVA-treated tumor tissues using liquid chromatography-mass spectrometry (LC-MS). These analyses revealed greater alterations in the purine synthesis pathways in AVA-resistant samples than in AVA-sensitive and vehicle-treated control samples (Figure 2A). Specifically, we found a greater abundance of metabolites such as urate, xanthine, xanthosine, and 3-ureidopropionate in the AVA-resistant group than in the control group (Figure 2B, $p < 0.05$ and Figure S3). We then performed desorption electrospray ionization mass spectrometry (DESI-MS) imaging^{34,35} of the same tumor tissues to further investigate treatment-specific metabolic changes within the heterogeneous TME. Spatially resolved molecular information was selectively extracted from the DESI-MS data obtained from tumor regions within each sample, excluding adjacent stroma or necrotic tissue. Significant alterations in the relative abundance of a variety of molecular species were identified when comparing control to AVA-treated tumors, including multiple key intermediates in amino acid metabolism, glycolysis, and purine synthesis (Figure 2C, FDR < 0.05). Higher relative abundances of xanthine and hypoxanthine were detected in AVA-resistant tumor tissue regions relative to control, in agreement with LC-MS experiments (Figure 2B and 2C; $p < 0.01$ and $p < 0.03$, respectively). Additionally, significant alterations in glutaminolysis metabolites were identified with increased relative abundances of glutamate relative to glutamine in AVA-resistant compared to AVA-sensitive tissues, but not when compared to control (normalized ion abundance: 7.4 vs. 5.3 and 9.1, respectively; Figures 2D and S1, $p < 0.05$). Similar trends were observed for fumarate and glutathione, both of which are downstream metabolites of glutamate. Overall, our comprehensive mass spectral analyses of AVA-treated tumors indicate a significant role of glutamine metabolism in these tumors.

Hypoxia induces GLS expression in a hypoxia-inducible factor-1 α -dependent manner

We next set out to further investigate the mechanisms by which GLS expression is altered after exposure to AVA therapy. In many cancers, GLS expression is correlated with HIF-1 α expression.^{33,36,37} To determine whether this is a direct correlation, we analyzed OVCAR8 ovarian cancer cells and RF24 endothelial cells that were transiently transfected with small interfering RNA (siRNA) targeting HIF-1 α or HIF-2 α (Figure 3A). We observed that increased GLS expression under hypoxic conditions (1% O₂) was abrogated by HIF-1 α siRNA but not by HIF-2 α or non-targeting siRNA ($p < 0.001$). These data indicate that enhanced upregulation of GLS in hypoxic conditions occurs in a HIF-1 α -dependent manner.

GLS is ubiquitously expressed in both ovarian cancer and endothelial cell lines

Before performing additional *in vitro* experiments to assess the effects of GLS inhibition on ovarian cancer and endothelial cell lines, we first confirmed GLS expression in the ovarian cancer cell lines A2780, HeyA8, SKOV3, OVCAR3, OVCAR4, OVCAR5, OVCAR8, OVCA432, and IGROV (Figure 3B). We cultured the cells under normoxic conditions and measured GLS protein and mRNA expression in them (Figure 3B). GLS expression levels were highest in the SKOV3 cells; therefore, we chose this cell line for further

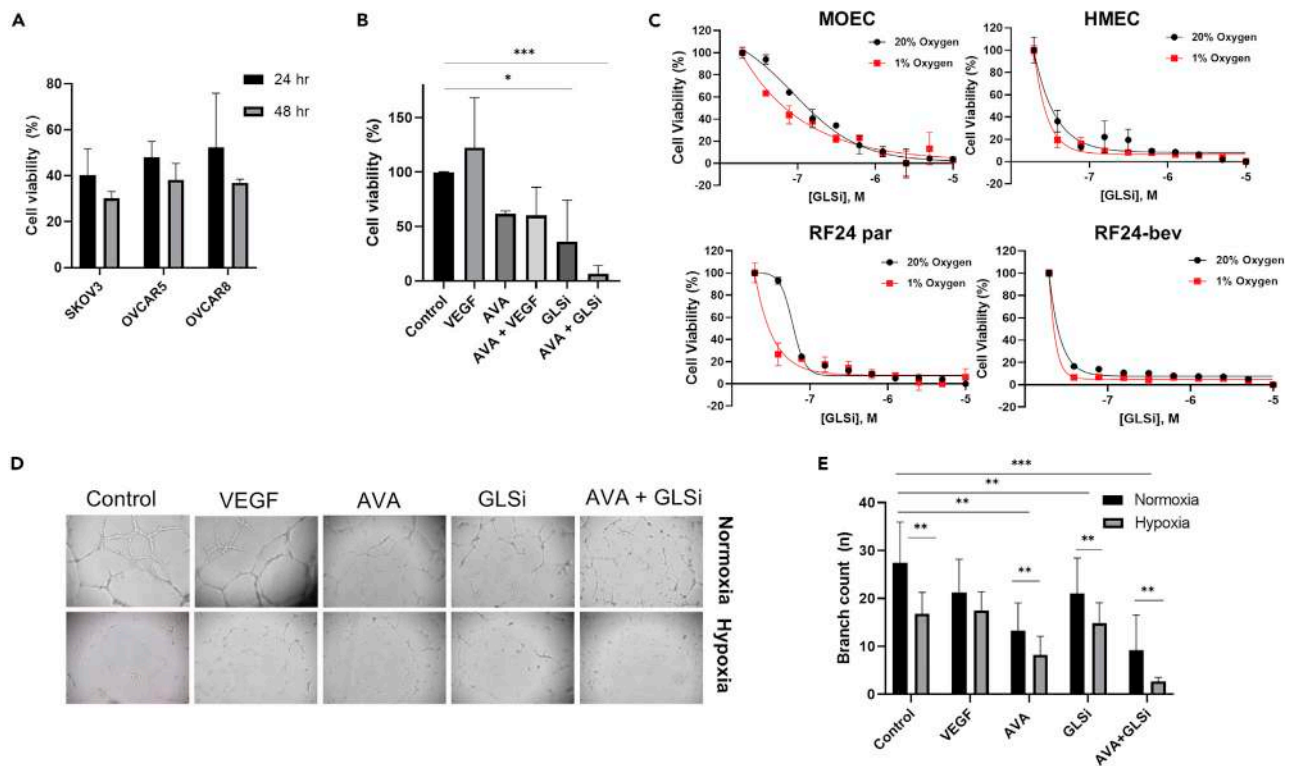


Figure 4. Hypoxia enhances sensitivity to GLS inhibition in both cancer and endothelial cells in vitro

(A) The viability of three ovarian cancer cell lines (SKOV3, OVCAR5, and OVCAR8) upon culture with GLSi alone for 24–48 h in normoxic conditions ($p < 0.05$). (B) The viability of the RF24 endothelial cell line after culturing with a positive control (VEGF), bevacizumab (AVA), GLSi monotherapy, or a combination of both therapies for 24 h in normoxic conditions ($*p < 0.05$, $***p < 0.001$). (C) The viability of four endothelial cell lines (MOEC, HMEC, parental RF24, and RF24-bev) after culturing in increasing concentrations of GLSi in either normoxic (20% O₂) or hypoxic (1% O₂) conditions. (D) Bright-field microscopic images at 50X showing the vessel loop formation and the effect of bevacizumab (AVA) and GLSi monotherapy or in combination (AVA + GLSi) on the angiogenic capability of RF24-par cells in culture in normoxia (top row) versus hypoxia (bottom row). (E) Average branch counts of the vessel loops described in the tube formation assay in (D) detected at 6 h as measured in triplicate experiments; $**p < 0.01$, $***p < 0.001$. VEGF, vascular endothelial growth factor; AVA, anti-VEGF antibody; GLSi, glutaminase inhibitor.

demonstrating that GLSi in combination with bevacizumab had a significantly greater reduction in tube formation than control therapy or monotherapy with either GLSi or bevacizumab (branch count 2.6 vs. 16.8, 14.9, and 8.2, respectively; $p \leq 0.001$). Ultimately, we observed increased sensitivity of both ovarian cancer and endothelial cell lines to GLSi therapy under hypoxic conditions, an effect that was even more pronounced when combined with AVA, and particularly in the endothelial cells that were resistant to AVA.

GLSi has robust antitumor effects in combination with AVA in vivo

To further assess the *in vitro* findings of increased GLSi sensitivity in hypoxia for both ovarian cancer and endothelial cells, we performed an *in vivo* experiment with an orthotopic SKOV3ip1 ovarian cancer mouse model. In this experiment, we randomized 60 nude mice to receive treatment with a vehicle control, GLSi, AVA, or a combination of AVA and GLSi given at the same doses as in monotherapy (Figure 5A). After seven weeks of treatment, the group of mice treated with the combination of AVA and GLSi exhibited a robust antitumor effect, with a lower mean tumor weight (0.05 g vs. 0.62 g and 0.64 g; $p < 0.01$) and tumor nodule number (3.3 vs. 12.8 and 13.9; $p < 0.05$) than those in the control and GLSi monotherapy groups, respectively (Figure 5B). The mean body weights were not significantly different between the combination therapy, GLSi monotherapy, and control groups (23.6 g, 22.0 g, and 22.1 g, respectively; $p = 0.16$, Figure S4). The mean tumor vessel density, as assessed by IHC staining for CD31, an endothelial cell marker, in the combination therapy group was lower than those in the control, GLSi monotherapy, and AVA monotherapy

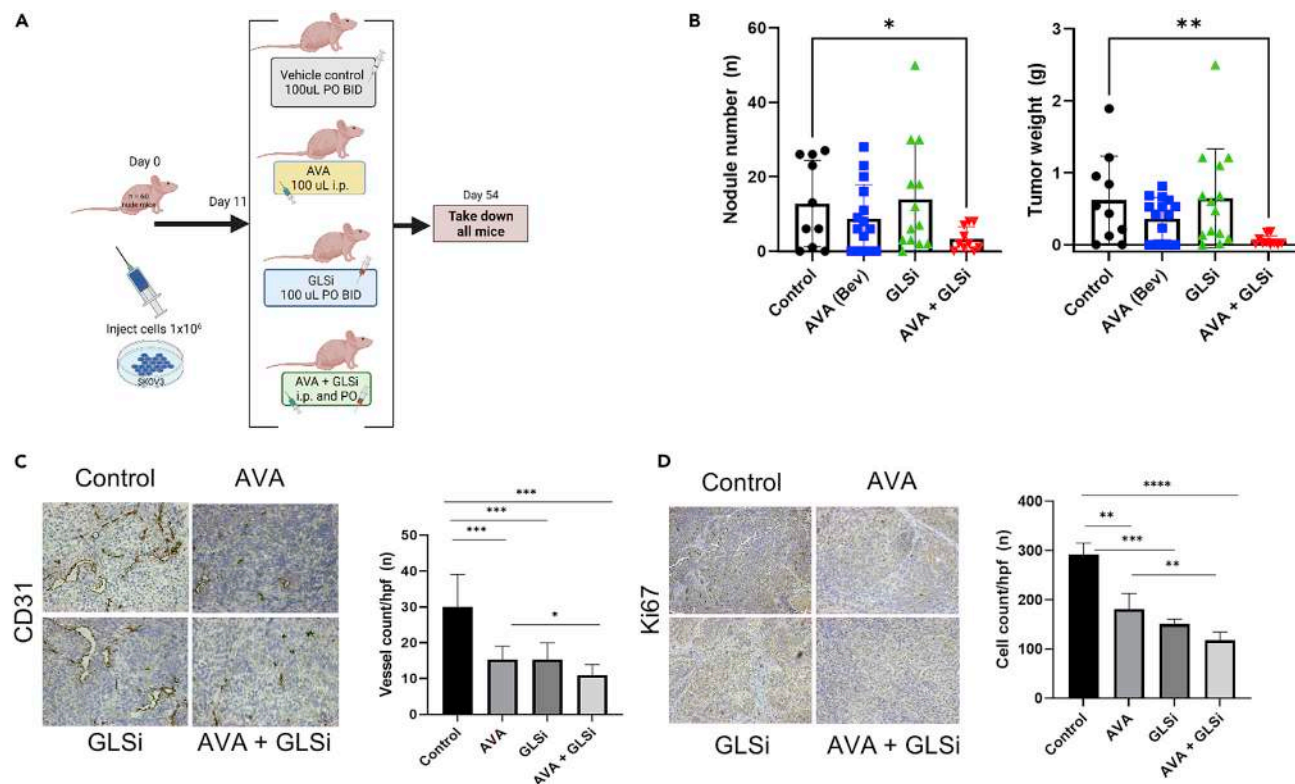


Figure 5. Robust antitumor effect of GLSi combined with AVA in an SKOV3ip1 mouse model as assessed using gross necropsy and immunohistochemistry

(A) *In vivo* schema of experimental protocol.

(B) Nodule numbers and tumor weights of SKOV3ip1 mouse model after either no treatment (Control), bevacizumab (AVA), IACS-012031 (GLSi), or a combination of bevacizumab and GLSi (AVA + GLSi). Error bars, SD. * $p < 0.05$; ** $p < 0.01$ (compared with the control group using the Student's *t* test).

(C) Blood vessel densities in ovarian tumor tissues harvested from mice in each treatment group as assessed by endothelial cell marker CD31. * $p < 0.05$; *** $p < 0.001$.

(D) Cell proliferation assay according to immunohistochemistry staining of mouse ovarian cancer tissues stained with anti-Ki67. ** $p < 0.01$, *** $p < 0.001$, **** $p < 0.0001$.

groups (11 vs. 30, 15, and 15, respectively; $p < 0.001$, Figure 5C). The tumors in the combination group also exhibited less cell proliferation than those in the GLSi and bevacizumab monotherapy treatment groups or control groups, respectively, as assessed using Ki67 staining (mean cell count/hpf: 108 vs. 151, 200, and 292; $p < 0.01$, Figure 5D).

We also subjected a subset of tissues obtained from this experiment ($n = 5$ per treatment group) to DESI-MS imaging analysis to investigate treatment-specific alterations. The relative abundances of 74 m/z features were significantly altered among treatment groups, corresponding to a broad range of small metabolites and lipid species (Figure S2, FDR < 5%). In particular, an overall reduction in the relative abundances of glutamate, malate, and hexose was identified in the combination therapy group compared to the control or monotherapy groups with either GLSi or AVA, respectively (normalized ion abundance 9.2, 13.1, 11.2 vs. 16.3, respectively; $p < 0.05$, Figures 6A and 6B). The relative abundances of glutamine and citrate were significantly increased in the GLSi monotherapy and combination groups compared to the control and AVA monotherapy groups (normalized ion abundance 13.4 and 9.0 vs. 1.9 and 3.6, respectively $p < 0.0001$, Figure 6B). When evaluating the conversion of pyruvate to lactate in the treatment groups, we observed a reduced relative abundance of lactate relative to pyruvate in all treatment groups compared to control, but most notably in the GLSi monotherapy and combination therapy groups, suggesting that the most substantial impact arising from GLSi therapy is on lactate metabolism (70.9, 72.6, 85.7 vs. 101.4, $p < 0.05$, Figures 6C and 6D).

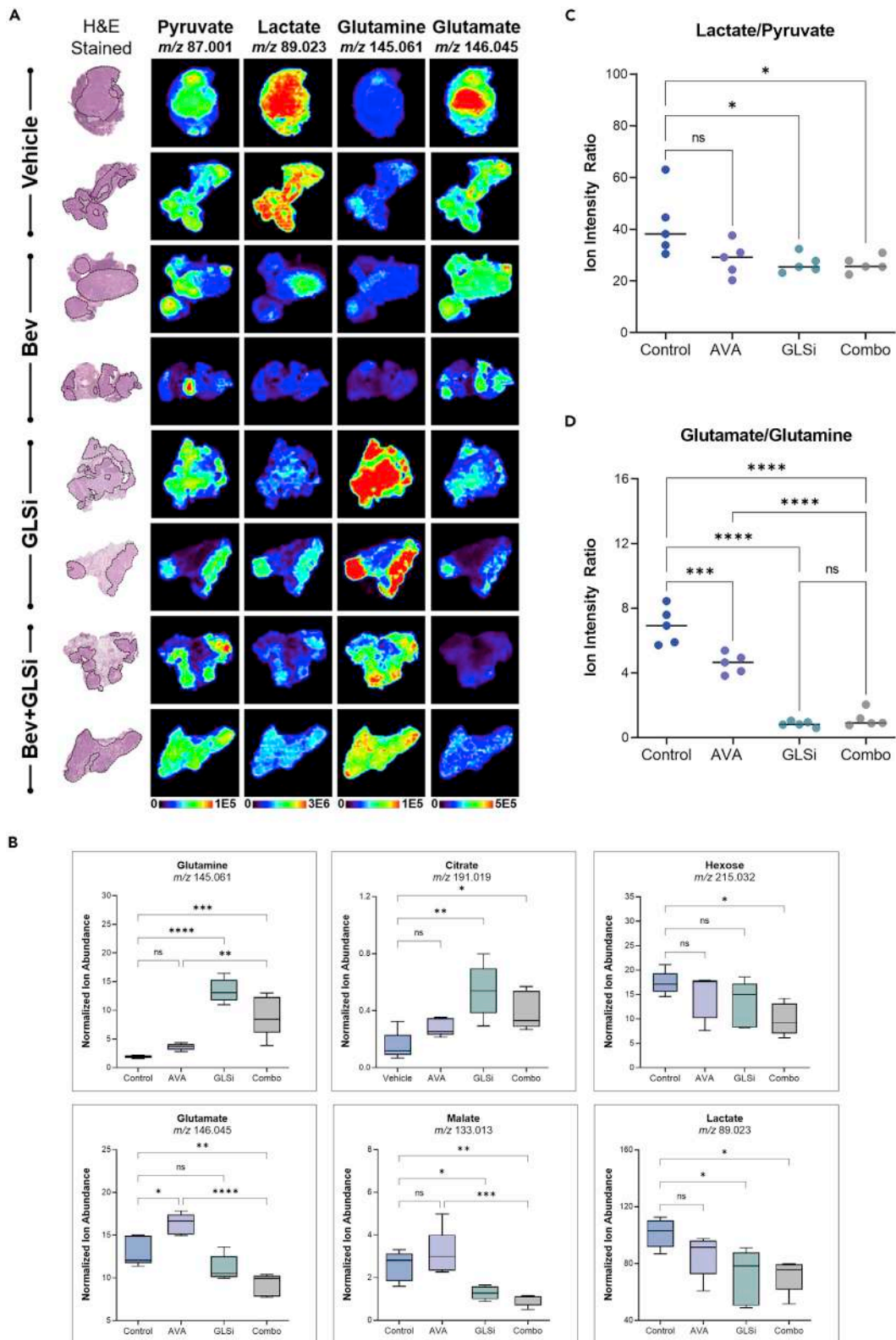


Figure 6. GLSi therapy has robust antitumor effects in combination with bevacizumab (AVA)

(A) Representative DESI-MS ion images of pyruvate, lactate, glutamine, and glutamate in mouse tumors after treatment with a control vehicle, AVA, GLSi, or a combination of the two. H&E, hematoxylin and eosin.

(B) Median normalized intensity of the relative abundance of glutamate metabolism and TCA cycle intermediates in control, AVA monotherapy, GLSi monotherapy, and combination therapy groups (Combo) mice in the SKOV3ip1 orthotopic ovarian cancer model. * $p < 0.05$, ** $p < 0.01$, *** $p < 0.001$, **** $p < 0.0001$.

(C) Median normalized intensity of the lactate-to-pyruvate ratio in the control and treatment groups. * $p < 0.05$; ns, not significant.

(D) Median normalized intensity ratio of glutamate to glutamine in the control, AVA monotherapy, GLSi monotherapy, and combination therapy treatment groups. Statistical significance was determined by Tukey's HSD test, *** $p < 0.001$, **** $p < 0.0001$.

Detection of GLSi therapy response using hyperpolarized magnetic resonance spectroscopy

To more accurately assess the therapeutic efficacy of GLSi therapy, we performed hyperpolarized magnetic resonance spectroscopy (HP-MRS) to quantify metabolic changes in lactate metabolism associated with this therapy in real time. We did so using a total of 10 mice from the aforementioned SKOV3ip1 model of adaptive resistance of ovarian cancer to AVA therapy, with five mice receiving a vehicle control and five receiving GLSi. HP-MRS is a novel technique that enhances the sensitivity of traditional magnetic resonance imaging up to 10,000-fold and facilitates a direct, noninvasive analysis of the flux of pyruvate metabolism with spatial resolution of tumors *in situ*.⁴⁰ Baseline MRI images were obtained with mice under anesthesia to confirm tumor location in both groups. After tail vein injection of hyperpolarized [$1\text{-}^{13}\text{C}$] pyruvate as outlined in the Materials and Methods, we quantitatively calculated each tumor's normalized lactate over pyruvate ratio, defined as the ^{13}C resonance signal of lactate divided by the ^{13}C resonance signal of pyruvate. Our analysis demonstrated that pyruvate-to-lactate conversion in AVA-resistant tumors was significantly reduced *in vivo* by GLSi therapy (0.337 vs. 0.178; $p \leq 0.001$, Figures 7A and 7B). These findings are concordant with the changes in relative abundance measured for pyruvate and lactate using DESI-MS imaging discussed above (Figure 6C).

GLS inhibition at the emergence of AVA resistance restores sensitivity in an adaptive resistance model of ovarian cancer

After observing the robust antitumor effects of GLSi combined with AVA therapy when given in combination up front, we set out to determine whether GLSi can restore sensitivity of ovarian cancer to AVA therapy if initiated after AVA resistance is established. For this experiment, we again used the SKOV3ip1 orthotopic mouse model but administered AVA monotherapy with bevacizumab after tumor establishment and continued it until resistance was confirmed by bioluminescent imaging (Figure 7C). Afterward, we maintained all AVA-resistant mice on AVA therapy and subsequently randomized them to receive either a vehicle control or GLSi (both at 200 μL via oral gavage twice a day) until they became moribund. GLSi therapy after establishment of adaptive resistance to AVA therapy resulted in a partial abrogation of tumor growth as evidenced by a 57% reduction in mean tumor weight (0.43 g vs. 1.01 g; $p = 0.04$) and a 68% lower mean tumor nodule number in the GLSi group than in the control group (5 vs. 15; $p = 0.0003$, Figure 7D). The administration of GLSi therapy after the emergence of AVA resistance not only provided an antitumor response but it also resulted in a significant survival benefit (mean survival 69 vs. 63 days; $p = 0.048$). Continuing AVA therapy in the resistant setting with a vehicle control was associated with a 2-fold increased risk of death compared to treatment with AVA plus GLSi (HR 2.07; 95% CI 1.03–4.15; Figure 7E).

DISCUSSION

Overall, the key finding of our investigation is that increased glutamine metabolism is a metabolic adaptation that occurs in an orthotopic ovarian cancer model of adaptive resistance to AVA therapy. We exploited this metabolic vulnerability of glutamine dependence by combining AVA therapy (bevacizumab) with GLSi which produced robust antitumor efficacy in both *in vitro* and *in vivo* models of ovarian cancer.

Reliance on glutamine metabolism for growth and development is an established hallmark of cancer.³ However, the fate of glutamine and its metabolism is complex.⁴¹ Previously, we reported the adaptive nature of the TME under nutrient stress, and in particular, we elucidated the role of reactive stromal cells under glutamine deprivation and the ability of malignant tumors to harness carbon and nitrogen from alternative sources to maintain glutamine stores.⁴² Use of these glutamine stores is heterogeneous, as they can be consumed during protein synthesis, serve as building blocks for the antioxidant glutathione, or be converted into α -ketoglutarate for tricarboxylic acid cycle anaplerosis via GLS.^{41,43} The role of GLS in cancer growth and progression varies among human cancers and is dependent on the cancer

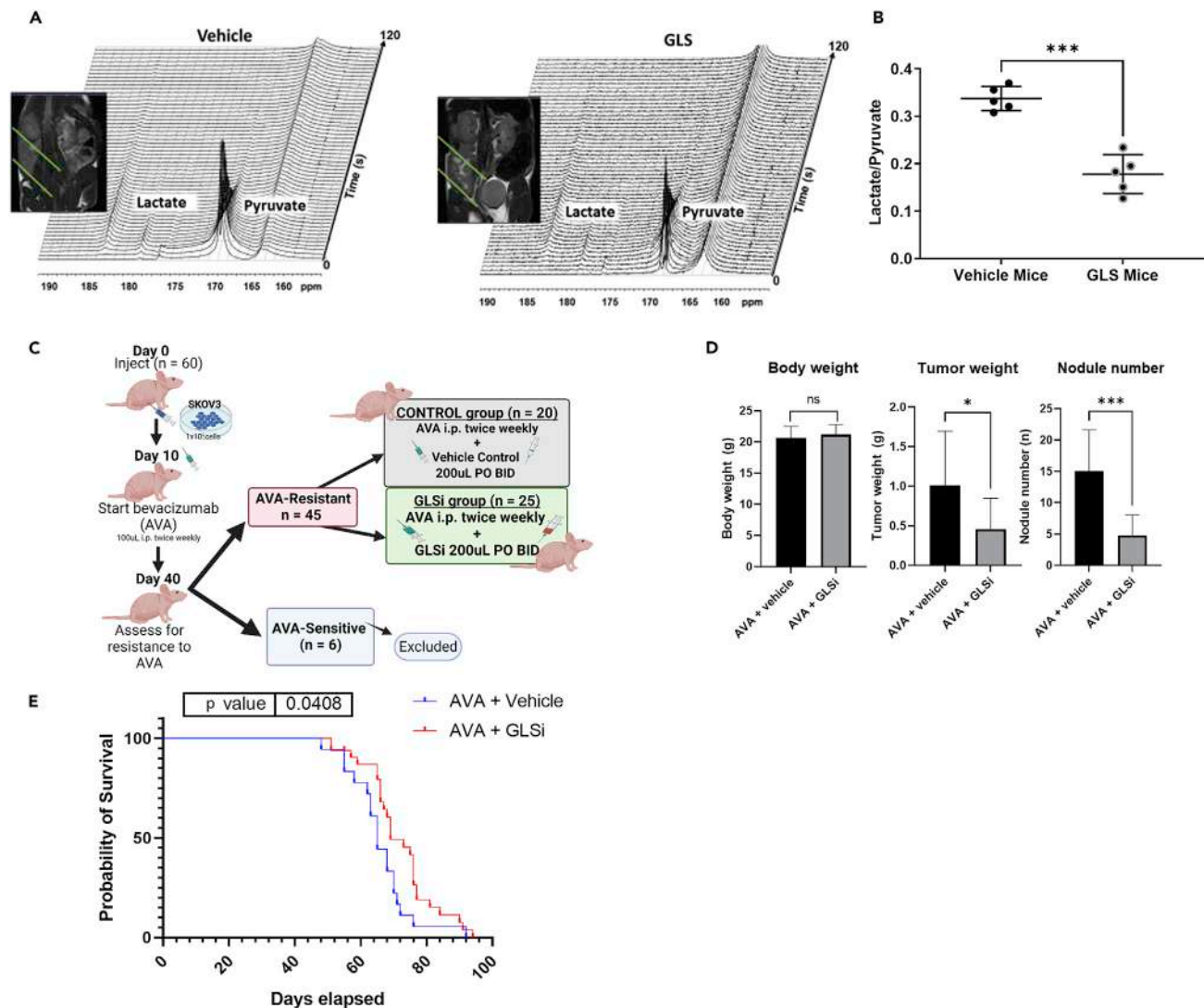


Figure 7. Detection of GLSi therapy response by HP-MRS and evaluating changes in AVA sensitivity when GLSi is given after emergence of AVA resistance

(A) Representative T2-weighted MRI (coronal slice) and real-time ^{13}C magnetic resonance spectroscopy images of AVA-resistant ovarian tumors in mice after intravenous hyperpolarized pyruvate injection for two treatment groups: vehicle control (left) and GLSi (right) with spectra collected from the MRI slabs on the ovarian tumors over 2 s.

(B) The normalized lactate/pyruvate ratios for vehicle- and GLSi-treated mice. *** $p < 0.001$.

(C) Schema of the orthotopic SKOV3ip1 mouse model in which AVA resistance was established prior to the initiation of GLSi therapy. AVA, anti-VEGF antibody, (bevacizumab).

(D) Body weights, tumor weights, and nodule numbers at the time of necropsy for mice treated with AVA combined with a vehicle vs. those given AVA combined with GLSi. Error bars, SD. * $p < 0.05$; *** $p < 0.001$ (compared with the control group using the Student's *t* test). ns, not significant.

(E) Kaplan-Meier survival curve showing survival advantage with GLSi therapy after AVA resistance is established ($p = 0.048$, HR 2.07; 95% CI 1.03–4.15). AVA, anti-VEGF antibody, (bevacizumab); GLSi, glutaminase inhibitor.

phenotype, with strong evidence of an oncogenic role for GLS in colon, liver, and ovarian cancers but not in other cancers, such as non-small-cell lung cancer.⁴¹ Thus, GLS expression and the prognostic implications of its expression vary by cancer type, with higher GLS expression associated with worse prognosis for ovarian cancer.³⁶

Since the U.S. Food and Drug Administration approved the AVA, bevacizumab, for use in patients with ovarian cancer in 2014, modest improvements in the progression-free survival of this cancer have

occurred.^{6–8} Subsequently, bevacizumab was approved for patients with relapsed ovarian cancer.⁹ These broad categories of approval translate into the reality that nearly every patient receiving treatment for ovarian cancer will be exposed to AVA with bevacizumab. Unfortunately, due in part to the metabolic adaptations discussed above, the benefits of bevacizumab are modest and adaptive resistance develops nearly universally within months of initiation. Therefore, additional agents are needed to target the population with adaptive resistance of ovarian cancer to AVA therapy.

In the present study, we identified ubiquitous expression of GLS in ovarian cancer cell lines and confirmed that treatment with bevacizumab is associated with an upregulation of GLS as a metabolic adaptation by both cancer cells and endothelial cells. This upregulation occurs in an HIF-1 α -dependent fashion in both ovarian cancer cells and endothelial cells where bevacizumab functions. We targeted this hypoxia-mediated increase in GLS expression using GLSi therapy. *In vitro*, we observed significant vulnerability of both cancer cells and endothelial cells to GLSi treatment, with increased sensitivity to GLSi treatment in the bevacizumab-resistant RF24 cells (RF24-bev). We subsequently noted a profound antitumor effect of GLSi in the SKOV3ip1 ovarian cancer orthotopic mouse model of adaptive resistance to bevacizumab suggesting that this combination of therapy may be of clinical benefit. Interestingly, we demonstrated antitumor efficacy of GLSi when given together with bevacizumab as up-front therapy and also demonstrated a survival benefit when GLSi was added to bevacizumab after the emergence of resistance. This suggests that GLSi therapy is of value when given in combination or sequentially with bevacizumab. Therefore, GLSi therapy may prove to be beneficial for patients whose disease relapses after exposure to bevacizumab or is AVA resistant. Our *in vivo* studies suggest that this combination therapy is well tolerated. Further investigations evaluating biologic markers that could predict response of ovarian cancer to GLSi therapy as well as evaluating the combination of GLSi with additional chemotherapy drugs are warranted.

Limitations of the study

Limitations of this study include the utilization of a single ovarian cancer cell line for the *in vivo* investigations. However, the authors selected the SKOV3ip1 ovarian cancer cell line due to the expression profile of GLS making it the most suitable candidate for study. Additionally, while the study provided a well-rounded assessment of metabolic adaptations of ovarian cancer cell lines and tumors exposed to hypoxic environments and GLSi treatment, definitive evaluation of the mechanisms of resistance and therapy response(s) were limited and merit further investigation.

Conclusion

GLSi therapy, when combined with AVA therapy, has robust antitumor effects in preclinical ovarian cancer models both *in vitro* and *in vivo*. This combined therapy warrants further exploration given the potential to expand the utility and efficacy of bevacizumab in treatment of ovarian cancer, particularly in the AVA-resistant setting.

STAR★METHODS

Detailed methods are provided in the online version of this paper and include the following:

- KEY RESOURCES TABLE
- RESOURCE AVAILABILITY
 - Lead contact
 - Materials availability
 - Data and code availability
- EXPERIMENTAL MODEL AND SUBJECT DETAILS
 - Cell lines and culture conditions
 - *In vivo* models of ovarian cancer
- METHOD DETAILS
 - Cell viability assay
 - Western blotting
 - Quantitative RT-PCR (qRT-PCR)
 - GLS gene silencing by small interfering RNA
 - IHC staining
 - Polar metabolite extraction from tissue

- LC-MS protocol and data analysis
- DESI-MS imaging and SAM analysis
- Hyperpolarized ¹³C-pyruvate sample preparation
- Animal handling during magnetic resonance imaging experiments
- T2-weighted proton MRI
- *In vivo* ¹³C magnetic resonance spectroscopy
- **QUANTIFICATION AND STATISTICAL ANALYSIS**

SUPPLEMENTAL INFORMATION

Supplemental information can be found online at <https://doi.org/10.1016/j.isci.2023.106020>.

ACKNOWLEDGMENTS

The research reported here is funded by the following: T32 training grant CA101642 (D.G.); MD Anderson Cancer Center Support Grant CA016672; CPRIT grant PR 180381; National Institutes of Health/National Cancer Institute grants award numbers P30 CA016672, R01 CA227622 (D.N. and A.K.S.), CA177909 (A.K.S.), R35 CA209904 (A.K.S.), MD Anderson Ovarian Cancer Moon Shot (A.K.S.), SPORE in Ovarian Cancer CA 217685 (A.K.S.), the American Cancer Society, the Dunwoody Fund, the Gordon Fund, and the Ovarian Cancer Research Alliance FP00006137 (E.S.). Shared resources utilized for the project include the small animal imaging facility (SAIF) and research histology core laboratory (RHCL). J.K. and M.S. provided the GLS inhibitor along with insights into formulation for its use in the *in vivo* experiment and contributed thoughtful discussion of the study design as well as manuscript review. Editorial support was provided by Don Norwood of MD Anderson Editing Services, Research Medical Library.

AUTHOR CONTRIBUTIONS

D.G. and A.K.S. were responsible for conceptualization, data curation, formal analysis, investigation, visualization, methodology, and manuscript writing, review, and editing. M.S.K., M.T., K.I.F., E.B., Y.W., E.S., and L.S.M. helped in establishing and maintaining the mouse colony and performed necropsy and tissue analysis. P.B., P.D., and C.V.K. conceptualized, performed, and analyzed the hyperpolarized magnetic resonance spectroscopy experiments and reviewed the manuscript. D.N., O.A., J.H.J., A.A., A.J., P.K., M.N., and F.W. performed the LC-MS experiments and L.S.E., M.S., and S.B. performed the DESI-MS experiments and performed all analyses of the results and preparation of the images in the figures related to these data. S.L., T.A.Y., and S.N.W. provided guidance on experimental design and review of the manuscript. All authors read and approved the final manuscript.

DECLARATION OF INTERESTS

A.K.S. reports consulting for KIYATEC, Merck & Co., GSK, Onxeo, ImmunoGen, lylon, and AstraZeneca; being a stockholder in Bio-Path Holdings; and receiving research funding from MTrap. T.A.Y. reports AstraZeneca, Almac, Aduro, Artios, Athena, Atrin, AxioM, Bayer, Bristol Myers Squibb, Calithera, Clovis, Cybrexa, EMD Serono, F-Star, GLG, Guidepoint, Ignyta, I-Mab, ImmuneSensor, Jansen, Merck, Pfizer, Repare, Roche, Schrodinger, Seattle Genetics, Varian, Zai Labs, and ZielBio. T.A.Y. is also the Medical Director of the Institute for Applied Cancer Science where the glutaminase inhibitor IACS-012031 was developed. S.N.W. reports AstraZeneca, Bayer, Clovis Oncology, Cotinga Pharmaceuticals, GSK, Merco, Novartis, OncXerna, Roche/Genentech, Zentalis; and is a paid consultant for Agenus, AstraZeneca, Clovis Oncology, Eisai, EQRX, GSK, ImmunoGen, Lilly, Merck, Merco, Novartis, Pfizer, Roche/Genentech, Vincerx, and Zentalis. L.S.E. is an inventor in patents owned by Purdue Research Foundation related to desorption electrospray ionization mass spectrometry imaging technology and receives royalties from its commercialization. L.S.E. has received research funding from Merck and Thermo Fisher Scientific.

Received: March 2, 2022

Revised: September 19, 2022

Accepted: January 16, 2023

Published: January 19, 2023

REFERENCES

- Torre, L.A., Trabert, B., DeSantis, C.E., Miller, K.D., Samimi, G., Runowicz, C.D., Gaudet, M.M., Jemal, A., and Siegel, R.L. (2018). Ovarian cancer statistics, 2018. *CA Cancer J. Clin.* 68, 284–296. <https://doi.org/10.3322/caac.21456>.
- McKeown, S.R. (2014). Defining normoxia, physoxia and hypoxia in tumours-implications for treatment response. *Br. J. Radiol.* 87, 20130676. <https://doi.org/10.1259/bjr.20130676>.
- Hanahan, D., and Weinberg, R.A. (2011). Hallmarks of cancer: the next generation. *Cell* 144, 646–674. <https://doi.org/10.1016/j.cell.2011.02.013>.
- Seltzer, V., Batson, J.L., Drukker, B.H., Gillespie, B.W., Gossfeld, L.M., Grigsby, P.W., Harvey, H.A., Hendricks, C.B., Hummel, S., Makuch, R.W., et al. (1995). Ovarian-cancer - screening, treatment, and follow-up. *J. Am. Med. Assoc.* 273, 491–497. <https://doi.org/10.1001/jama.1995.03520300065039>.
- Jain, R.K. (2014). Antiangiogenesis strategies revisited: from starving tumors to alleviating hypoxia. *Cancer Cell* 26, 605–622. <https://doi.org/10.1016/j.ccr.2014.10.006>.
- Pujade-Lauraine, E., Hilpert, F., Weber, B., Reuss, A., Poveda, A., Kristensen, G., Sorio, R., Vergote, I., Witteveen, P., Bamias, A., et al. (2014). Bevacizumab combined with chemotherapy for platinum-resistant recurrent ovarian cancer: the AURELIA open-label randomized phase III trial. *J. Clin. Oncol.* 32, 1302–1308. <https://doi.org/10.1200/JCO.2013.51.4489>.
- Aghajanian, C., Blank, S.V., Goff, B.A., Judson, P.L., Teneriello, M.G., Husain, A., Sovak, M.A., Yi, J., and Nycum, L.R. (2012). OCEANS: a randomized, double-blind, placebo-controlled phase III trial of chemotherapy with or without bevacizumab in patients with platinum-sensitive recurrent epithelial ovarian, primary peritoneal, or fallopian tube cancer. *J. Clin. Oncol.* 30, 2039–2045. <https://doi.org/10.1200/JCO.2012.42.0505>.
- Perren, T.J., Swart, A.M., Pfisterer, J., Ledermann, J.A., Pujade-Lauraine, E., Kristensen, G., Carey, M.S., Beale, P., Cervantes, A., Kurzeder, C., et al. (2011). A phase 3 trial of bevacizumab in ovarian cancer. *N. Engl. J. Med.* 365, 2484–2496. <https://doi.org/10.1056/NEJMoa1103799>.
- F.D.A. (2018). Avastin (Bevacizumab) Information in Postmarket Drug Safety Information for Patients and Providers (U.S. Food & Drug Administration). www.fda.gov.
- Sennino, B., and McDonald, D.M. (2012). Controlling escape from angiogenesis inhibitors. *Nat. Rev. Cancer* 12, 699–709. <https://doi.org/10.1038/nrc3366>.
- Yang, L., Moss, T., Mangala, L.S., Marini, J., Zhao, H., Wahlig, S., Armaiz-Pena, G., Jiang, D., Achreja, A., Win, J., et al. (2014). Metabolic shifts toward glutamine regulate tumor growth, invasion and bioenergetics in ovarian cancer. *Mol. Syst. Biol.* 10, 728. <https://doi.org/10.1002/msb.20134892>.
- (2021). Glutaminase inhibitor CB-839 and azacitidine in treating patients with advanced myelodysplastic syndrome. <https://ClinicalTrials.gov/show/NCT03047993>.
- (2021). Testing whether cancers with specific mutations respond better to glutaminase inhibitor, telaglenastat hydrochloride, anti-cancer treatment, BeGIN study. <https://ClinicalTrials.gov/show/NCT03872427>.
- (2017). Study of the glutaminase inhibitor CB-839 in leukemia. <https://ClinicalTrials.gov/show/NCT02071927>.
- (2018). Study of the glutaminase inhibitor CB-839 in hematological tumors. <https://ClinicalTrials.gov/show/NCT02071888>.
- (2020). Study of the glutaminase inhibitor CB-839 in solid tumors. <https://ClinicalTrials.gov/show/NCT02071862>.
- (2021). KEAPSAKE: a study of telaglenastat (CB-839) with standard-of-care chemioimmunotherapy in 1L KEAP1/NRF2-mutated, nonsquamous NSCLC. <https://ClinicalTrials.gov/show/NCT04265534>.
- (2021). CB-839 HCl in combination with carfilzomib and dexamethasone in treating patients with recurrent or refractory multiple myeloma. <https://ClinicalTrials.gov/show/NCT03798678>.
- (2021). Study of CB-839 (telaglenastat) in combination with talazoparib in patients with solid tumors. <https://ClinicalTrials.gov/show/NCT03875313>.
- (2021). A study of telaglenastat (CB-839) in combination with palbociclib in patients with solid tumors. <https://ClinicalTrials.gov/show/NCT03965845>.
- (2021). Study CB-839 in combination with nivolumab in patients with melanoma, clear cell renal cell carcinoma (ccRCC) and non-small cell lung cancer (NSCLC). <https://ClinicalTrials.gov/show/NCT02771626>.
- (2017). A comparative, pharmacokinetic study of CB-839 capsule and tablet formulations in healthy adults. <https://ClinicalTrials.gov/show/NCT02944435>.
- (2021). Novel PET/CT imaging biomarkers of CB-839 in combination with panitumumab and irinotecan in patients with metastatic and refractory RAS wildtype colorectal cancer. <https://ClinicalTrials.gov/show/NCT03263429>.
- (2022). CB-839 with radiation therapy and temozolomide in treating patients with IDH-mutated diffuse astrocytoma or anaplastic astrocytoma. <https://ClinicalTrials.gov/show/NCT03528642>.
- (2021). Study of CB-839 in combination w/paclitaxel in patients of African ancestry and non-African ancestry with advanced triple negative breast cancer (TNBC). <https://ClinicalTrials.gov/show/NCT03057600>.
- (2021). Telaglenastat + talazoparib in prostate cancer. <https://ClinicalTrials.gov/show/NCT04824937>.
- (2021). Testing of the anti cancer drugs CB-839 HCl (telaglenastat) and MLN0128 (sapanisertib) in advanced stage non-small cell lung cancer. <https://ClinicalTrials.gov/show/NCT04250545>.
- (2021). IACS-6274 with or without pembrolizumab for the treatment of advanced solid tumors. <https://ClinicalTrials.gov/show/NCT05039801>.
- (2021). Telaglenastat hydrochloride and osimertinib in treating patients with EGFR-mutated stage IV non-small cell lung cancer. <https://ClinicalTrials.gov/show/NCT03831932>.
- (2021). CANTATA: CB-839 with cabozantinib vs. cabozantinib with placebo in patients with metastatic renal cell carcinoma. <https://ClinicalTrials.gov/show/NCT03428217>.
- (2021). CB-839 in combination with niraparib in platinum resistant BRCA-wild-type ovarian cancer patients. <https://ClinicalTrials.gov/show/NCT03944902>.
- (2021). Study to evaluate the ECG effects of telaglenastat in healthy adult subjects. <https://ClinicalTrials.gov/show/NCT04607512>.
- Koh, M.Y., and Powis, G. (2012). Passing the baton: the HIF switch. *Trends Biochem. Sci.* 37, 364–372. <https://doi.org/10.1016/j.tibs.2012.06.004>.
- Wiseman, J.M., Ifa, D.R., Song, Q., and Cooks, R.G. (2006). Tissue imaging at atmospheric pressure using desorption electrospray ionization (DESI) mass spectrometry. *Angew. Chem. Int. Ed. Engl.* 118, 7346–7350. <https://doi.org/10.1002/ange.200602449>.
- Eberlin, L.S., Ferreira, C.R., Dill, A.L., Ifa, D.R., Cheng, L., and Cooks, R.G. (2011). Nondestructive, histologically compatible tissue imaging by desorption electrospray ionization mass spectrometry. *Chembiochem* 12, 2129–2132. <https://doi.org/10.1002/cbic.201100411>.
- Xiang, L., Mou, J., Shao, B., Wei, Y., Liang, H., Takano, N., Semenza, G.L., and Xie, G. (2019). Glutaminase 1 expression in colorectal cancer cells is induced by hypoxia and required for tumor growth, invasion, and metastatic colonization. *Cell Death Dis.* 10, 40. <https://doi.org/10.1038/s41419-018-1291-5>.
- Buffa, F.M., Harris, A.L., West, C.M., and Miller, C.J. (2010). Large meta-analysis of multiple cancers reveals a common, compact and highly prognostic hypoxia metagene. *Br. J. Cancer* 102, 428–435. <https://doi.org/10.1038/sj.bjc.6605450>.
- Wu, C., Chen, L., Jin, S., and Li, H. (2018). Glutaminase inhibitors: a patent review. *Expert Opin. Ther. Pat.* 28, 823–835. <https://doi.org/10.1080/13543776.2018.1530759>.

39. Gross, M.I., Demo, S.D., Dennison, J.B., Chen, L., Chernov-Rogan, T., Goyal, B., Janes, J.R., Laidig, G.J., Lewis, E.R., Li, J., et al. (2014). Antitumor activity of the glutaminase inhibitor CB-839 in triple-negative breast cancer. *Mol. Cancer Ther.* **13**, 890–901. <https://doi.org/10.1158/1535-7163.mct-13-0870>.
40. Wang, Z.J., Ohliger, M.A., Larson, P.E.Z., Gordon, J.W., Bok, R.A., Slater, J., Villanueva-Meyer, J.E., Hess, C.P., Kurhanewicz, J., and Vigneron, D.B. (2019). Hyperpolarized C-13 MRI: state of the art and future directions. *Radiology* **291**, 273–284. <https://doi.org/10.1148/radiol.2019182391>.
41. Cluntun, A.A., Lukey, M.J., Cerione, R.A., and Locasale, J.W. (2017). Glutamine metabolism in cancer: understanding the heterogeneity. *Trends Cancer* **3**, 169–180. <https://doi.org/10.1016/j.trecan.2017.01.005>.
42. Yang, L., Achreja, A., Yeung, T.L., Mangala, L.S., Jiang, D., Han, C., Baddour, J., Marini, J.C., Ni, J., Nakahara, R., et al. (2016). Targeting stromal glutamine synthetase in tumors disrupts tumor microenvironment-regulated cancer cell growth. *Cell Metab.* **24**, 685–700. <https://doi.org/10.1016/j.cmet.2016.10.011>.
43. Wise, D.R., and Thompson, C.B. (2010). Glutamine addiction: a new therapeutic target in cancer. *Trends Biochem. Sci.* **35**, 427–433. <https://doi.org/10.1016/j.tibs.2010.05.003>.
44. Langley, R.R., Fan, D., Tsan, R.Z., Rebhun, R., He, J., Kim, S.J., and Fidler, I.J. (2004). Activation of the platelet-derived growth factor-receptor enhances survival of murine bone endothelial cells. *Cancer Res.* **64**, 3727–3730. <https://doi.org/10.1158/0008-5472.CAN-03-3863>.
45. Livak, K.J., and Schmittgen, T.D. (2001). Analysis of relative gene expression data using real-time quantitative PCR and the 2(T)(-Delta Delta C) method. *Methods* **25**, 402–408. <https://doi.org/10.1006/meth.2001.1262>.
46. Landen, C.N., Chavez-Reyes, A., Bucana, C., Schmandt, R., Deavers, M.T., Lopez-Berestein, G., and Sood, A.K. (2005). Therapeutic EphA2 gene targeting in vivo using neutral liposomal small interfering RNA delivery. *Cancer Res.* **65**, 6910–6918.
47. Zhou, Q., Zhu, C., Shen, Z., Zhang, T., Li, M., Zhu, J., Qin, J., Xie, Y., Zhang, W., Chen, R., et al. (2020). Incidence and potential predictors of thromboembolic events in epithelial ovarian carcinoma patients during perioperative period. *Eur. J. Surg. Oncol.* **46**, 855–861. <https://doi.org/10.1016/j.ejso.2020.01.026>.
48. Tusher, V.G., Tibshirani, R., and Chu, G. (2001). Significance analysis of microarrays applied to the ionizing radiation response. *Proc. Natl. Acad. Sci. USA* **98**, 5116–5121. <https://doi.org/10.1073/pnas.091062498>.

STAR★METHODS

KEY RESOURCES TABLE

REAGENT or RESOURCE	SOURCE	IDENTIFIER
Antibodies		
Rat anti-mouse CD31 monoclonal antibody	BD Pharmingen	Cat. #553370; RRID: AB394816
Rabbit anti-mouse CA9 monoclonal antibody	Novus Biologics	Cat. # NB100-417SS; RRID: AB_788423
Goat anti-rat horseradish peroxidase-linked secondary antibody	Jackson ImmunoResearch	Cat. # 112-035-167; RRID: AB_2338139
Rabbit anti-mouse Ki67 monoclonal antibody	NeoMarkers	Cat. # RB-9043-P1; RRID: AB_149873
Chemicals, peptides, and recombinant proteins		
Lipofectamine 2000	Invitrogen	Cat # 11668030
Hank's Balanced Salt Solution	Cellgro	Cat. # 21-021-CV
Luciferin	GoldBio	Cat. # LUCK-1G
2-hydroxypropyl-beta-cyclodextrin	Sigma-Aldrich	Cat. # H107-100G
DAB	Invitrogen	Cat. # 750118
¹³ C pyruvic acid	ISOTEC; Sigma-Aldrich	Cat. # 677175
Glutaminase inhibitor (GLSi)	IACS	IACS-012031
Critical commercial assays		
BCA Protein Assay Kit	Thermo Fisher Scientific	Cat. # 23225
Western Lightning PLUS ECL Kit	PerkinElmer	Cat. # NEL103E001EA
RNeasy Mini Kits	Qiagen	Cat. # 74004
High-Capacity cDNA Reverse Transcription Kit	Applied Biosystems, Inc.	Cat. # 4368814
Experimental models: Cell lines		
Human: RF24	Courtesy of Dr. Lee Ellis	CVCL_AX74
Human: SKOV3ip1	ATCC	CVCL_0C84
Human: OVCAR8	MDACC cell line bank	CVCL_1629
Human: OVCAR5	ATCC	CVCL_1628
Human: HeyA8	MDACC cell line bank	CVCL_8878
Human: A2780	MDACC cell line bank	CVCL_0134
Human: OVCAR3	MDACC cell line bank	CVCL_0465
Human: OVCAR 4	MDACC cell line bank	CVCL_1627
Human: IGROV	MDACC cell line bank	CVCL_8723
Human: HMEC	ScienCell Research Laboratories	Cat. # 1000
Murine: MOEC	Courtesy of Dr. Robert Langley ⁴⁴	Courtesy of Dr. Robert Langley ⁴⁴
Experimental models: Organisms/strains		
Mouse: athymic nude female (NCR-nude)	Taconic Biosciences	Model # NCRNU-F
Oligonucleotides		
Human-specific GLS siRNA (GAGGAAAAGGUUGCAUGAUUAdtdT)	Proteintech	Cat. # 12855-1-AP
Control-non-targeting siRNA (UAAUCUGCAACCUUCCUCTdT)	Sigma-Aldrich (St. Louis, MO)	Cat. # SIC001
MISSION siRNA Universal Negative Control #1	Sigma-Aldrich	Cat. # SIC0012NMOL
Software and algorithms		
GraphPad Prism v 9.3.0	GraphPad Software, Inc., San Diego, CA	https://www.graphpad.com/

(Continued on next page)

Continued

REAGENT or RESOURCE	SOURCE	IDENTIFIER
ImageJ	NIH Image	https://imagej.nih.gov/ij/inex.html
MATLAB	The MathWorks	https://www.mathworks.com/
Xenogen IVIS imaging system	PerkinElmer	https://www.perkinelmer.com/product/ivis-lumina-s5-imaging-system-cls148588

RESOURCE AVAILABILITY

Lead contact

Further information and requests for resources and reagents should be directed to and will be fulfilled by the Lead Contact, Anil. K. Sood, M.D. (asood@mdanderson.org).

Materials availability

All unique/stable reagents generated in this study are available from the [lead contact](#) with a completed Materials Transfer agreement.

Data and code availability

- Any additional information required to reanalyze the data reported in this paper is available from the [lead contact](#) upon request.
- This paper does not report original code.

EXPERIMENTAL MODEL AND SUBJECT DETAILS

Cell lines and culture conditions

The human ovarian cancer cell lines SKOV3ipluc (RRID: CVCL_0C84), OVCAR5 (RRID: CVCL_1628), and OVCAR8 (RRID: CVCL_1629) were obtained from the ATCC and The University of Texas MD Anderson Cancer Center Cytogenetics and Cell Authentication Core. The immortalized human vascular endothelial cell line RF24 (RRID: CVCL_AX74) was obtained from Dr. Lee Ellis. The murine ovarian endothelial cells (MOEC) were obtained from Dr. Robert Langley and have been previously characterized and described.⁴⁴ Human microvascular endothelial cells (HMEC) were purchased from ScienCell Research Laboratories (Carlsbad, CA) and maintained according to the manufacturer's instructions with endothelial cell medium (ScienCell) containing 10% fetal bovine serum. For *in vitro* studies, HMECs were treated and applied to MTT and Western blot analysis between 5 and 8 passages. SKOV3ipluc and OVCAR8 cells were cultured in RPMI 1640 medium (HyClone) supplemented with 10% fetal bovine serum (Sigma-Aldrich) and 1% gentamycin. OVCAR5 cells were cultured in Dulbecco's modified Eagle's medium supplemented with 10% fetal bovine serum and 1% gentamycin. RF24 cells were cultured in minimum essential medium supplemented with 10% fetal bovine serum, sodium pyruvate, non-essential amino acids, and 1% gentamycin. MOEC cells were cultured in phenol red free DMEM supplemented with 10% fetal bovine serum and 0.1% gentamicin sulfate. All cells were cultured at 37°C with 5% CO₂ with the exception of MOEC which were cultured at 33°C. All cells were cultured at ambient atmospheric O₂ with the exception of hypoxia experiments in which case they were cultured 1% O₂, as indicated. All cell lines were authenticated by the Cytogenetics and Cell Authentication Core using short tandem repeat fingerprinting and were tested for mycoplasma contamination using polymerase chain reaction. Cells were used within 20 passages after thawing for *in vitro* experiments and 10 passages after thawing for *in vivo* experiments. *In vitro* studies were done with 70-80% confluent cultures.

In vivo models of ovarian cancer

All animal protocols were approved by the MD Anderson Institutional Animal Care and Use Committee. All animal experiments were performed with 6- to 8-week-old female athymic nude mice (NCR-nude) obtained from Taconic Biosciences. The mice were housed five per cage under pathogen-free conditions at a constant temperature and humidity. All mice were fed a regular diet and water *ad libitum* according to the guidelines of the American Association for Laboratory Animal Science and the U.S. Public Health Service Policy on Humane Care and Use of Laboratory Animals. Investigators sacrificed the mice via carbon dioxide euthanasia followed by cervical dislocation once the mice were moribund.

To establish xenograft models for all mouse experiments, luciferase-labeled SKOV3ip1 ovarian cancer cells were cultured to 70–90% confluence and then trypsinized, washed twice with phosphate-buffered saline, and resuspended in ice-cold Hank's Balanced Salt Solution (cat. #21-021-CV; Cellgro). The mice were then inoculated with 1×10^6 SKOV3ip1 cells via intraperitoneal injection to the right side of the abdomen. Tumor establishment was subsequently confirmed after injection of 200 μ L of 14.3 mg/mL luciferin (cat. #LUCK-1G; GoldBio) using a Xenogen IVIS *in vivo* imaging system. Following confirmation of disease burden (mice without tumor uptake were removed from the experiment), all mice in the therapeutic experiment were randomly assigned to the following treatment groups: vehicle control, bevacizumab (anti-human VEGF antibody, AVA, at 6.25 mg/kg, intraperitoneally, twice a week), GLSi (IACS-012031, 200 mg/kg given orally twice daily, five days a week), or a combination of the two at these doses ($n = 15$ for all groups). In the AVA-resistance model, twice-weekly treatment with AVA (bevacizumab) was initiated upon confirmation of tumor uptake. Tumor burden was subsequently assessed weekly via IVIS imaging (Xenogen), and the mice were placed in two groups: therapy-sensitive and -resistant. Sensitivity to AVA therapy was defined as a decrease or plateau in the relative intensity of bioluminescent signaling over three weeks of treatment. The therapy-sensitive mice were sacrificed approximately one week later to confirm that they truly had sensitive phenotypes. Resistance to AVA therapy was defined as an initial decrease then steady increase in the relative intensity of bioluminescent signaling. The resistant group was then separated into two groups: control (AVA plus vehicle control given via oral gavage twice a day, $n = 20$) and treatment (AVA plus GLSi given via oral gavage twice a day, $n = 25$). The treatment in both groups continued until each mouse became moribund and then were sacrificed. The mice were monitored daily for adverse effects of treatment, and their body weights were measured weekly. Survival time was calculated for each mouse as the number of days from the date of inoculation of SKOV3ip1 cells to the date of euthanasia.

Mouse tumor weights, nodule numbers, distribution of metastasis, and presence of ascites were recorded at the time of gross necropsy. All tumor tissues were dissected, and samples were snap-frozen for later protein or RNA analysis (e.g., DESI-MS, LC-MS), fixed in formalin for paraffin embedding, or snap-frozen in optimal cutting temperature compound (Mercedes Scientific) for frozen slide preparation.

Bevacizumab was obtained from MD Anderson. The glutaminase inhibitor, IACS-012031, was obtained from the MD Anderson Institute for Applied Cancer Science and reconstituted in 25% aqueous 2-hydroxypropyl- β -cyclodextrin (cat. #H107-100G; Sigma-Aldrich) in phosphate-buffered saline at a dose of 25 mg/mL. This was administered via oral gavage as above. Once mice in any group became moribund, all the mice were euthanized.

METHOD DETAILS

Cell viability assay

To evaluate the cytotoxic effects of GLSi and bevacizumab monotherapy and in combination on cell viability, ovarian cancer cells (SKOV3ip1, OVCAR5, and OVCAR8) were seeded in a 96-well plate at a density of 3,000 cells per well in a 100- μ L total volume in quadruplicates. Cells were incubated for 24 hours, and after demonstration of adequate attachment, the culture medium was removed and replaced with a medium containing serial dilutions of GLSi and bevacizumab. The cells were then incubated for 24, 48, or 72 hours depending on the experimental oxygen conditions. Following incubation, the cells were treated with a 0.05% MTT solution for 2–4 hours. The supernatant was then gently removed, and the MTT formazan was dissolved in 100 μ L of dimethyl sulfoxide. The absorbance was subsequently read at 570 nm using a BioTek uQuant microplate spectrophotometer. All experiments were performed in triplicate. Dose-response curves were plotted using Prism software (version 8.0.0; GraphPad Software).

Western blotting

Extraction of total protein cell lysates was performed using modified RIPA buffer with protease and phosphatase inhibitors. BCA Protein Assay Reagent (Thermo Fisher Scientific) was then used to measure protein concentrations. Protein expression for each lysate was subsequently detected via Western blotting of a 10% sodium dodecyl sulfate-polyacrylamide gel electrophoresis separation gel using a primary antibody against GLS (cat. #12855-1-AP; Proteintech). The antibody was incubated overnight at 4°C and then incubated with corresponding horseradish peroxidase-linked whole secondary antibodies. A chemiluminescence assay using a Western Lightning PLUS ECL Kit (PerkinElmer) was performed to expose the

membranes and protein bands were quantified using densitometry with ImageJ software (National Institutes of Health). β -actin was used as a sample loading control for all reads.

Quantitative RT-PCR (qRT-PCR)

Relative levels of mRNA expression of GLS were detected using the qRT-PCR method as described before.¹¹ Briefly, each qRT-PCR was carried out with 1 μ g of RNA isolated from cells using RNeasy Mini Kits (Qiagen, CA) and reverse transcribed using High-Capacity cDNA Reverse Transcription Kit (Applied Biosystems Inc.) according to the manufacturer's protocol. The cDNA synthesized was then used as a template in the qRT-PCR using the specific GLS TaqMan Gene expression probe (Hs0104020_m1, ThermoFisher). Quantitative RT-PCR was performed on a 7500 Real-Time PCR System (Applied Biosystems, Inc.). The 18s rRNA was used as endogenous control, and relative mRNA expression was calculated using $2^{-\Delta\Delta CT}$ method.⁴⁵

GLS gene silencing by small interfering RNA

Small interfering RNA (siRNA) targeted to GLS was purchased from Sigma-Aldrich. *In vitro* transient transfection was performed as described previously.⁴⁶ Briefly, the cells were transfected with a GLS1-specific or scrambled (control) siRNA using lipofectamine 2000 reagent (Invitrogen, Carlsbad, CA). siRNA with a nonspecific function that shared no sequence homology with any known mammalian mRNA in a BLAST search was used to control the target siRNA (Mission siRNA Universal Negative Control#1, Sigma). At selected time intervals, cells were harvested to measure mRNA levels of *GLS1* using qRT-PCR.

IHC staining

All tumor samples subjected to IHC staining were collected from the *in vivo* experiment. Formalin-fixed, paraffin-embedded tumor sections were used for staining for anti-Ki67 (1:100, cat #RB-9043-PI; NeoMarkers). Paraffin slides were prepared via deparaffinization and antigen retrieval, whereas frozen slides were prepared via cold acetone fixation. This was followed by endogenous peroxidase blocking with 3% hydrogen peroxide and a protein block with 4% fish gelatin. All samples were incubated with a primary antibody diluted in 4% fish gelatin overnight and then incubated with either a peroxidase-conjugated goat anti-rabbit or anti-mouse secondary antibody for one hour at room temperature.

Frozen slides were used for staining for CD31 (1:800, cat. #53370; BD Pharmingen) and CA9 (1:100, cat# NB100-417SS; Novus Biologicals) using goat anti-rat and goat anti-rabbit horseradish peroxidase-linked secondary antibodies, respectively (1:250, cat. #112-035-167; Jackson ImmunoResearch). Frozen slides were prepared by first fixing slides in cold acetone for 10 minutes and then washing them in phosphate-buffered saline and blocking with endogenous peroxidase and 3% H₂O₂ in methanol. All samples were incubated with a primary antibody diluted in protein block (5% normal horse serum and 1% normal goat serum in phosphate-buffered saline) overnight at 4°C. The slides were then incubated with a secondary antibody for one hour and then incubated with DAB (Invitrogen, Cat. #750118). Microscopic assessment of DAB staining was performed for all slides to monitor appropriate staining density. The slides were counterstained with hematoxylin (Gill 3). Quantification of IHC staining was performed by randomly selecting five fields at 200x magnification per slide and manually counting stained nuclei in each field. Mean cell counts and SDs were calculated, and treatment groups were compared using the Student *t*-test.

Polar metabolite extraction from tissue

The protocol was modified from Zhou et al.⁴⁷ To minimize metabolite degradation tumor tissue samples were kept on dry ice throughout the LC-MS experiment. Briefly, 30–66 mg of each tissue sample was quickly weighed in a homogenizer tube previously filled with beads. A prechilled methanol/water (1:1, v/v) solution was added to the tube based on the weight of the measured tissue (5 mL per 1 g of tissue, or 125 μ L per 25 mg of tissue). The samples were then homogenized using a Precellys homogenizer (Bertin Instruments) at 4°C and 6,500 rpm using two cycles of 25 seconds with 30-second intervals. Afterward, 100 μ L of the tissue homogenate was transferred to a fresh tube, and 500 μ L of methanol/water (1:1, v/v) solution and 500 μ L of chloroform were added to the samples and they were vortexed for two minutes at 4°C and centrifuged at 16,000 g for 10 minutes at 4°C. A total of 500 μ L of polar metabolite extract was then dried in a vacuum evaporator. The dried metabolites were reconstituted in 200 μ L of methanol/water (1:1, v/v) solution, sonicated for 10 minutes, and filtered through an Agilent 0.2- μ m Econofilter. The filtrate was then transferred into LC vials for analysis.

LC-MS protocol and data analysis

A 10- μ L tumor sample prepared in the manner outlined above was injected for analysis into an Agilent 6520 Q-TOF LC/MS machine with an ACQUITY UPLC BEH C18 Column (130 Å, 1.7 μ m, 2.1 mm \times 150 mm) coupled with VanGuard Pre-Columns and an XBridge BEH Amide XP Column (130 Å, 2.5 μ m, 4.6 mm \times 150 mm) coupled with an XBridge BEH Amide XP VanGuard Cartridge (130 Å, 2.5 μ m, 2.1 mm \times 5 mm). The column compartment was set at 40°C, and the analysis was performed in both positive and negative modes. One hundred microliters of sample filtrated was transferred to LC vials, and 10 μ L of each filtered sample was pooled to form the quality control samples. For analysis of the C18 column, mobile phase A consisted of water with 0.1% formic acid, whereas mobile phase B contained acetonitrile in 0.1% formic acid. The gradient method using the C18 column was as follows: 0 minutes: 1% B; 1 minute: 1% B; 8 minutes: 99% B; 13 minutes: 85% B; 13.1 minutes: 1% B; 16 minutes: 1% B. For analysis with the HILIC column, the mobile phase A was 10 mM ammonium formate in water with 0.1% formic acid, whereas mobile phase B contained 10 mM ammonium formate in acetonitrile with 0.1% formic acid. The gradient method using the HILIC column was as follows: 0 minutes: 99% B; 11.8 minutes: 20% B; 12.5 minutes: 99% B; 14.7 minutes: 99% B. The metabolite peaks were extracted for the analysis using Agilent MassHunter Profinder software based on our in-house library of metabolites. Any metabolites whose relative SD was greater than 30% in the QC measurements were excluded from further analysis. The metabolite peak areas in the spectrum were normalized according to the weight of the tissue. Other downstream analyses were performed using MetaboAnalyst software version 5.0 and data were then presented with the aid of GraphPad Prism version 8.0.0.

DESI-MS imaging and SAM analysis

Tumor tissues were flash-frozen and stored at -80°C prior to analysis. Frozen tissues were sectioned at 12 μ m thickness, thaw-mounted onto glass slides, and immediately analyzed using a Q Exactive Focus or Q Exactive HF Orbitrap mass spectrometer (Thermo Fisher Scientific) coupled to a 2D OmniSpray stage (Prosolia Inc.) and a laboratory-built DESI sprayer. DESI-MS imaging was performed in the negative ion mode at a spatial resolution of 200 μ m using a mass resolving power of 70,000 (m/z 200) and an instrument method optimized for enhanced detection of small metabolite species from m/z 80–500. A histologically compatible solvent system comprised of methanol:acetone 4:1 (v/v) was used as the DESI spray solvent, at a flow rate of 5.0 μ L/min. DESI-MS ion images were assembled and visualized using Firefly (Prosolia, Inc.) and BioMap (Novartis) software. Ions of interest were tentatively identified using high mass accuracy measurements and tandem mass spectrometry experiments.

After DESI-MS imaging, the analyzed tissue sections were stained with hematoxylin and eosin and regions of tumor, stroma, and necrosis were annotated by D.G. within each sample. Mass spectra were extracted from pixels corresponding to tumor regions within the DESI-MS dataset using MSiReader software. The resulting ion intensity matrix was processed by binning each m/z value to the nearest thousandth and removing peaks that were present in less than 20% of the extracted pixels. The extracted DESI-MS data was analyzed using significance analysis of microarrays (SAM), a modified significance test to identify statistically significant alterations in relative abundance for specific mass-to-charge (m/z) values.⁴⁸ Multiclass SAM was performed in R using the "samr" package to identify features with significantly altered abundance among treatment groups. A false discovery rate (FDR) of 5% was applied to identify m/z values with significant differences in relative abundance among treatment groups. Ion intensities for selected metabolites of interest were plotted in GraphPad Prism (version 9.3.0) and subjected to one-way ANOVA with Tukey's post-hoc test for pairwise comparisons.

Hyperpolarized ^{13}C -pyruvate sample preparation

A solution of 20 μ L of ^{13}C pyruvic acid (ISOTEC; Sigma-Aldrich), 15 mM OX63 trityl radical (GE Healthcare), and 1.5 mM gadolinium chelate (ProHance) was polarized at 3.35 T and 1.4 K using dynamic nuclear polarization (HyperSense; Oxford Instruments) for one hour. A frozen ^{13}C -pyruvate sample was rapidly dissolved in 4 mL of superheated alkaline buffer containing 100 mg/L EDTA, 40 mM NaOH, 40 mM TRIS buffer, and 30 mM NaCl. The final concentration of pyruvate injected into the mouse tail vein was 80 mM, with a physiologic pH of about 7.4. Next, 200 μ L of hyperpolarized pyruvate was injected into mice using a tail vein catheter for 8–10 seconds.

Animal handling during magnetic resonance imaging experiments

For magnetic resonance imaging (MRI) experiments, a 7T Bruker BioSpin MRI scanner (horizontal bore) was used. Mice were anesthetized using isoflurane in an anesthesia chamber with scavenging. The animals were fixed in a holder specially designed for mice and placed in the MRI coil equipped with a nose cone for inhaled anesthesia. A respiration monitoring pad and body temperature-maintaining heated pad were used during the MRI experiments.

T2-weighted proton MRI

Conventional anatomic magnetic resonance images of mice were acquired using multislice T2-weighted rapid acquisition with a relaxation enhancement sequence. Images with different views, including axial, coronal, and sagittal views, were acquired to identify tumors and regions of interest in the flanks of the mice. The imaging parameters for the T2-weighted scans were an echo time of 15 ms, repetition time of 2.5 seconds, 4-cm field of view, 256 μm \times 256 μm in-plane resolution, 10 slices with thicknesses of 1 mm, and four image averages.

In vivo ^{13}C magnetic resonance spectroscopy

A series of slab-selective ^{13}C spectra with a slab thickness of 8 mm was acquired right after injection of mice with hyperpolarized pyruvate using an SP Flash sequence. The subcutaneous tumor locations and similar sizes of the tumors in the experimental mice used in this study increased the precision of slab placement through most of the ovarian tumors and limited the contribution of nonmalignant signals consistently throughout the experiments. A total of 90 transients were acquired using a delay time between each transient of two seconds (total time, three minutes). For each transient, a 15° flip angle excitation Gaussian pulse and 2,048 data points were used. A small 8 M ^{13}C urea phantom injected with gadolinium-DPTA was used in each mouse experiment for chemical shift referencing. Experimental data were processed on the MATLAB programming language (The MathWorks, Inc.) and TopSpin (Bruker BioSpin) platforms. Phase correction and 10- to 15-Hz line broadening were introduced to each individual spectrum. The areas under the spectral peaks within the frequency range for pyruvate and lactate were integrated over the entire array. The lactate-to-pyruvate metabolic flux ratios (lactate/pyruvate) were estimated by calculating the individual integration of lactate and pyruvate spectral signals between treatment groups and comparing the change in signal over time.

QUANTIFICATION AND STATISTICAL ANALYSIS

Differences between groups were evaluated using the Student *t*-test or Mann-Whitney U test according to data distribution and variance homogeneity. One-way differences between two groups were evaluated using the Student *t*-test or Mann-Whitney U test according to data distribution and variance homogeneity, whereas one-way analysis of variance was used for multiple group comparison. For survival experiments, Kaplan-Meier analysis and a log-rank test were performed to explain differences in survival. All statistical analyses were conducted using Prism software (version 8.0.0). The *p* values were two-tailed and values less than 0.05 were considered significant. All results were presented as means (\pm SEM or SD).